THE MICROSCOPE SPACE MISSION TO TEST THE EQUIVALENCE PRINCIPLE

Gilles Metris, Manuel Rodrigues, Joël Berge

SF2A 2023
M. N'Diaye, A. Siebert, N. Lagarde, O. Venot, K. Baillié, M. Béthermin, E. Lagadec, J. Malzac, J. Richard (eds)

THE MICROSCOPE SPACE MISSION TO TEST THE EQUIVALENCE PRINCIPLE

G. MÉTRIS[1], M. RODRIGUES[2] and J. BERGÉ[2]

Abstract. The MICROSCOPE mission tested the Weak Equivalence Principle (WEP) with an unprecedented precision of order 10^{-15}, two orders of magnitude better than the previous best lab experiments. While the WEP, the cornerstone of General Relativity (GR), does not sway, the decade-long problems faced by fundamental physics stay still: how can we unify GR with the Standard Model, and how can we explain the acceleration of the cosmological expansion? As most beyond-GR models predict a violation of the WEP, albeit at an unknown level, it remains critical to even better test the WEP. In this paper, we review the MICROSCOPE mission, give its final constraint on the WEP, and build on its experimental limitations to show how we could improve them by a further two-order of magnitude in the precision of the test of the WEP.

Keywords: Equivalence Principle, Differential accelerometer, Space Experiment, Eötvös ratio

1 Introduction

The universality of free-fall (UFF) has been recognised since Galileo rolled objects down inclined planes and found that, locally, they all undergo the same gravitational acceleration: all objects within the same gravitational field fall at the same rate, independently of their mass and composition. With Newton's second law, the UFF can be restated as the proportionality between the gravitational mass m_G and the inertial mass m_I, with the same proportionality constant for all bodies: this is the usual definition of the weak equivalence principle (WEP). The Equivalence Principle, as generalised by Einstein, was the starting point to general relativity (GR).

GR describes gravitation as the simple spacetime's curvature, while recovering Newton's description of gravitation as a classical inverse-square law force in weak gravitational fields and for velocities small compared to the speed of light. As a highly predictive theory, it has so far successfully passed all experimental tests (Will 2014; Ishak 2019). Standing next to GR, the Standard Model (SM) was built from the realisation that the microscopic world is intrinsically quantum.

Although both GR and SM leave few doubts about their validity in their respective regimes, scientists have been faced with difficulties for decades. Firstly, the question of whether GR and the SM should and could be unified remains open: major theoretical endeavours delivered models such as string theory, but still fail to provide a coherent vision of the world. Secondly, the unexpected dark matter and dark energy make up most of the Universe's mass-energy budget.

The WEP has been tested for four centuries with increased precision (Eötvös et al. 1922; Bessel 1832; Roll et al. 1964; Braginskii & Panov 1971; Schlamminger et al. 2008; Wagner et al. 2012; Williams et al. 2012; Viswanathan et al. 2018). The concept of a test in space emerged in the 1970s (Chapman & Hanson 1970; Everitt et al. 2003), motivated by the quiet environment that space can provide and by the benefit of test periods much longer than on-ground experiments. In 1999, ONERA (Office National d'Etudes et de Recherches Aérospatiales) and OCA (Observatoire de la Côte d'Azur) proposed the MICROSCOPE mission (MICRO-Satellite à Compensation de traînée pour l'Observation du Principe d'Equivalence) to CNES.

MICROSCOPE was finally launched in 2016. After successfully dealing with unexpected anomalies (Rodrigues et al. 2022a), the mission provided two and a half years of useful data. In 2017, a first analysis based on only 7% of the eventual science data allowed us to verify the WEP at 2×10^{-14} sensitivity level (Touboul et al. 2017, 2019). In 2022, the full data allowed us to improve that precision by one order of magnitude (Touboul et al. 2022a). In this paper, we first describe MICROSCOPE in Sect. 2. In Sect. 3, we describe the data processing and provide the upper bound provided by MICROSCOPE on the validity of the WEP.

[1] Université Côte d'Azur, Observatoire de la Côte d'Azur, CNRS, IRD, Géoazur, F-06560 Valbonne, France
[2] DPHY, ONERA, Université Paris Saclay, F-92322 Châtillon, France

2 MICROSCOPE mission overview

2.1 WEP test experiment principle

The measurement relies on comparing the accelerations of two concentric bodies – cylinders in the case of MICROSCOPE – in orbit around the Earth. As shown in Fig. 1, the measurement is performed along the cylinders' X-axis, which is aligned with their main axis. In an inertial pointing configuration, it is pointing in the same direction of the Earth's gravity field vector once per orbit. In a perfect case, the difference of acceleration is proportional to the Eötvös parameter defined by the relative ratio of difference of gravitational-to-inertial masses m_{gj}/m_{ij} between two materials j:

$$\delta(2,1) = 2\frac{a_2 - a_1}{a_2 + a_1} = 2\frac{m_{g2}/m_{i2} - m_{g1}/m_{i1}}{m_{g2}/m_{i2} + m_{g1}/m_{i1}}, \tag{2.1}$$

where a_j are the acceleration undergone by the two bodies.

In MICROSCOPE, the test-masses are part of a double concentric accelerometer. The test-masses are finely controlled by electrostatic forces to be motionless with respect to the surrounding electrodes as illustrated in the right panel of Fig. 1. The forces applied by the set of electrodes are determined by the voltage applied on the test-mass and on each electrodes(Liorzou et al. 2022). The combination of these voltages with the geometry of the instrument defines the electrostatic forces and torques applied to each test-mass in order to counteract all the other effects that prevent the test-mass to stay motionless with respect to the satellite.

Thus, if a WEP violation exists, it can be detected as a signal with a well-known frequency (the orbital frequency $f_{\rm orb}$ in the case of Fig. 1) in the differential acceleration measured by the accelerometer (i.e., the difference of electrostatic force per unit mass between the two test masses). The measurement precision can be improved by rotating the satellite about the axis normal to the orbital plane. This increases the modulation frequency of the Earth's gravity vector projected onto the X-axis, to put it closer to the minimum of the instrumental noise. The WEP-violation frequency becomes $f_{\rm EP} = f_{\rm orb} + f_{\rm spin}$, with $f_{\rm spin}$ the rotation frequency of the satellite. Two spin frequencies have been used during the mission, leading to two test measurement data sets at $f_{\rm EP} \approx 0.9 \times 10^{-3}$ Hz and $f_{\rm EP} \approx 3.1 \times 10^{-3}$ Hz.

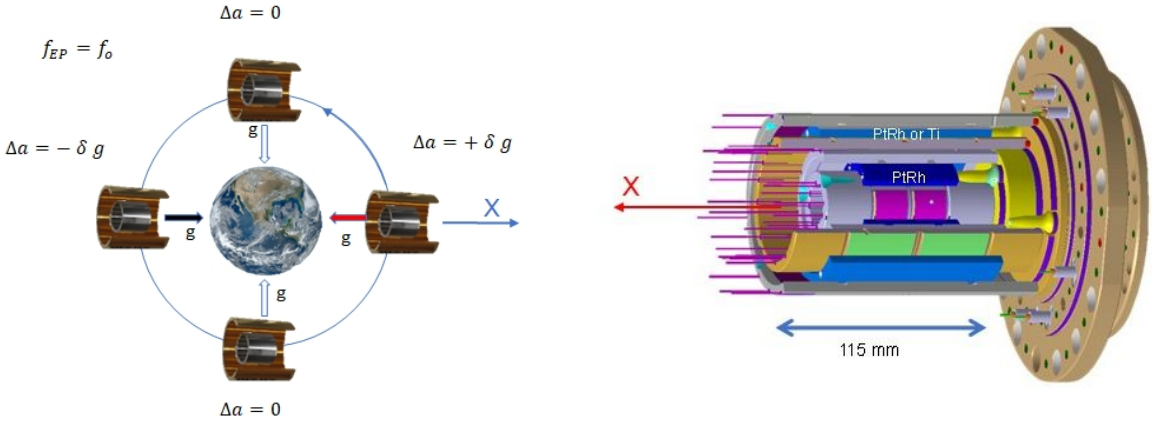

Fig. 1. Left: Experimental principle. **Right:** accelerometer core.

2.2 Payload

The payload (Liorzou et al. 2022) is composed of two identical differential accelerometers also called sensor units (SUs) except for the test-mass material. Each SU have two concentric hollow cylindrical test-masses surrounded by electrodes engraved on gold-coated silica parts. Each SU is connected to a front-end electronics unit (FEEU) which delivers the voltages to the test-masses and electrodes and transmits the data to the interface control unit (ICU). Each ICU connected to the FEEU contains all the digital electronics and software to operate the test-mass control servo-loops and data conditioning for the satellite and then the ground telemetry. The SU and the FEEU are integrated in a thermal cocoon placed at the core of the satellite which offers a micro-Kelvin stability around the measurement frequencies.

The first SU, called SUREF, comprises two test-masses of the same material: PtRh10 platinum-rhodium alloy containing 90% by mass of Pt ($A = 195.1$, $Z = 78$) and 10% Rh ($A = 102.9$, $Z = 45$). SUREF is dedicated to experiment and accuracy verification (in orbit or on ground within the data processing) as it is supposed to give a null signal at $f_{\rm EP}$. The second SU, called SUEP, comprises two test-masses of different material: the same PtRh10 alloy for the inner test-mass and an aeronautic titanium alloy (TA6V) for the outer test-mass with the atomic composition 90% of titanium ($A = 47.9$, $Z = 22$), 6% of aluminium ($A = 27.0$, $Z = 13$) and 4% of vanadium ($A = 50.9$, $Z = 23$). SUEP is dedicated to the WEP test.

2.3 Drag-free satellite

One of the challenges of the mission objectives is to make the satellite environment as quiet as possible for the payload to prevent any corruption of acceleration measurements.

The MICROSCOPE mission has been developed on the basis of scientific missions exploiting the CNES MYRIADE micro-satellite product line whose architecture comprises a platform with generic functional chains (energy, communication, computer, structure, etc.). Some adaptations and modifications were necessary to cope with the unusual performance requirements. Usually, the payloads of the MYRIADE satellites are located on the decoupled upper part of the platform but MICROSCOPE payload module has been accommodated at the centre of the spacecraft where it could take advantage of a more stable thermal environment (Fig. 2).

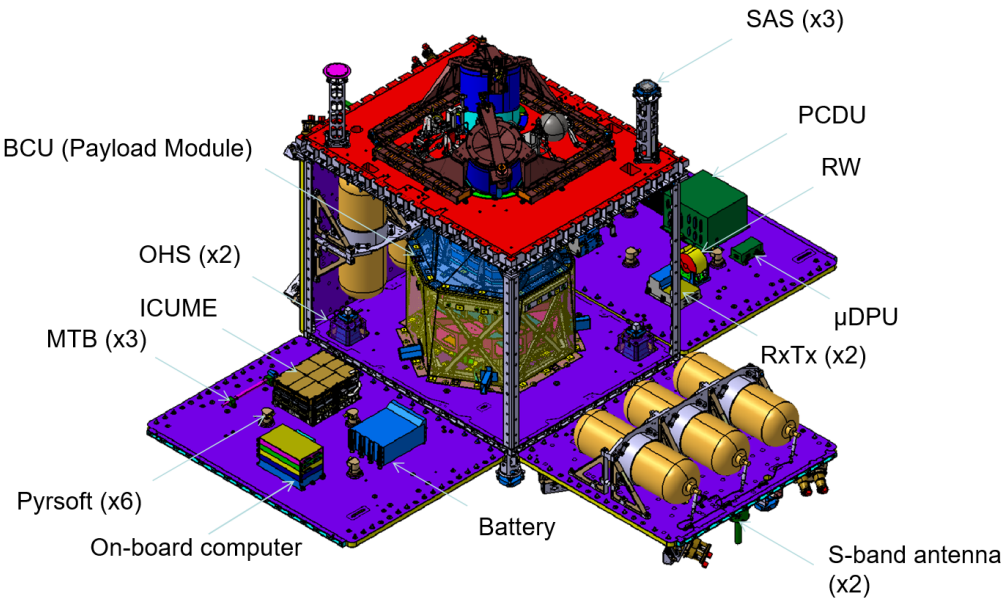

Fig. 2. The cube forming the satellite is open in the picture, the instrument T-SAGE is at the centre surrounded by the two 2×3 tanks of the cold gas propulsion system. Once closed the satellite cube measures $1.4\,\mathrm{m} \times 1\,\mathrm{m} \times 1.5\,\mathrm{m}$ and weighs about 300 kg.

The satellite thermal design has been optimised to offer the payload a tight temperature stability: the required stability around the WEP test frequency $f_{\rm EP}$ was set to 1 mK at the sensor unit interface and to 10 mK at the associated analog electronics interface. Active heaters did not operate during the science operations in order to avoid any interference with the payload measurements. Consequently, the thermal control on the satellite purely relied on passive methods: the dissipation of the electronic units was ensured by satellite external radiators. The in-orbit estimated thermal performance exceeded requirements and expectations. The payload was also shielded from the Earth and satellite magnetic field. In addition, the mechanical or electronic micro disturbances were minimised by a careful design and analysis to ensure an optimal environment: choice of multi-layer insulation (MLI) to minimise cracking, minimisation of current loops, study of thermoelastic deformations

to estimate internal gravitational effects...

To counteract non-gravitational forces and torques, an active control of accelerations and attitude of the satellite was implemented through the DFACS (Fig. 3). The DFACS used the scientific instrument itself as main sensor for delivering the linear as well as the angular accelerations hybridised with the star tracker measurements. The control laws for acceleration and attitude estimated the total forces and torques to be applied on the satellite which were transformed into eight micro-thrust commands sent to the cold gas propulsion system placed on two opposite walls of the satellite (Fig. 2). The DFACS in-orbit performances allowed to reduce the disturbances by 90 dB around $f_{\rm EP}$ leading to a controlled linear acceleration better than $3 \times 10^{-13}\,{\rm m\,s^{-2}}$, one order of magnitude better than expectation. The satellite attitude was controlled to better than 1 μrad at $f_{\rm EP}$ with an angular velocity stability better than $3 \times 10^{-10}\,{\rm rad\,s^{-1}}$ at $f_{\rm EP}$ in rotating mode, one order of magnitude better than expectation as well. The induced angular acceleration was controlled to better than $10^{-11}\,{\rm rad\,s^{-2}}$ at $f_{\rm EP}$, limiting centrifugal effects due to the off-centring of the test-masses.

Besides, the DFACS was able to receive additional external sine signals at particular frequencies in order to calibrate the instrument (differential scale factor, test-mass alignments and off-centerings, coupling between axes, non-linearity). Particular sessions were also dedicated to thermal sensitivities thanks to dedicated heaters.

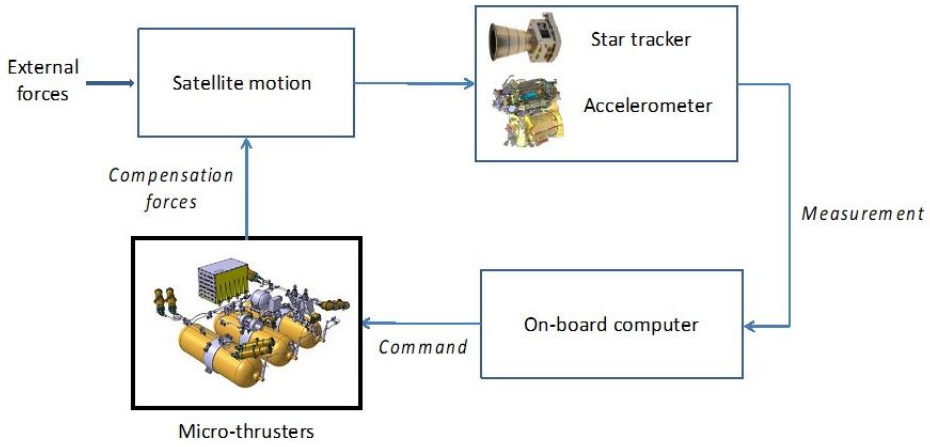

Fig. 3. Satellite Drag-Free and Attitude Control System

3 Data processing

3.1 Measurement equation

A single accelerometer (called inertial sensor) measures the difference of acceleration between the test-mass of the accelerometer and the centre of mass of the satellite. A differential accelerometer yields the difference $\vec{\Gamma}^{(d)} = \vec{\Gamma}^{(1)} - \vec{\Gamma}^{(2)}$ of two such accelerations for two test-masses. The accelerometers are not perfect, in the sense that we look for very small signals and thus any little defect can make deviate from an ideal response: they have bias, scale factors departing from unity, non-zero coupling between axes (Touboul et al. 2022c). Moreover, their orientation in the satellite, in space and with respect to the Earth's gravity field, is not perfectly known. That is why the measured differential acceleration $\vec{\Gamma}^{(d)}$ is not identical to the real one $\vec{\gamma}^{(d)}$, but is related to it as (Touboul et al. 2022c):

$$\vec{\Gamma}^{(d)} = \vec{b}_0^{(d)} + \left[\mathbf{A}^{(c)}\right] \vec{\gamma}^{(d)} + 2\left[\mathbf{A}^{(d)}\right] \vec{\gamma}^{(c)} + \vec{n}^{(d)}, \tag{3.1}$$

where

- $\vec{b}_0^{(d)}$ is the difference of bias between the two inertial sensors;
- $\left[\mathbf{A}^{(c)}\right]$ is the common mode sensitivity matrix, close to the identity matrix, which includes scale factors, coupling between axes and global rotation common to the two sensors;

- $\left[\mathbf{A}^{(d)}\right]$ is the differential mode sensitivity matrix, very small, which takes into account the difference of characteristics of the two sensors;
- $\vec{\gamma}^{(c)}$ is the common mode acceleration which is mainly due to residual non-gravitational accelerations acting on the satellite and not on the enclosed test-masses; these non-gravitational accelerations include drag and radiation pressures and the thrust applied to the satellite which is servo-controlled in order to considerably reduce $\vec{\gamma}^{(c)}$ in the frequency band of interest;
- $\vec{n}^{(d)}$ is the (coloured) noise.

The potential WEP-violation signal, $\delta(2,1)\vec{g}$, is included in $\vec{\gamma}^{(d)}$ which also contains the gravity gradient and the differential angular acceleration due to the small residual off-centring between the two test-masses (Rodrigues et al. 2022a):

$$\vec{\gamma}^{(d)} = \delta(2,1)\vec{g}(O_{\rm sat}) + ([\mathrm{T}] - [\mathrm{In}])\vec{\Delta} + \vec{b}_1^{(d)}, \tag{3.2}$$

where

- $\vec{g}(O_{\rm sat})$ is the gravity acceleration;
- [T] is the gravity gradient tensor;
- [In] is the gradient of inertia matrix;
- $\vec{\Delta}$ is the off-centring vector from the centre of test-mass (1) to the centre of test-mass (2);
- $\vec{b}_1^{(d)}$ contains the differences between the other small (mainly non gravitational) perturbations acting on the two test-masses.

Only the axis of the cylindrical test-masses, called X, which is much more precise than the other axes is used to estimate the EP signal. Therefore Eq. (3.1) has to be projected onto the X-axis. This leads to numerous terms Rodrigues et al. (2022a) but some are negligible and others are calibrated and corrected (Touboul et al. 2022b). The remaining model used to analyse the measurements along the X-axis reads

$$\Gamma^{(d)}_{x,\rm corr} = \sum_{j=0}^{3} \alpha_j (t-t_0)^j + \delta_x g_x + \delta_z g_z + \Delta'_x S_{xx} + \Delta'_z S_{xz} + n_x^{(d)}, \tag{3.3}$$

where

- $\delta_x \approx A^{(c)}_{(1,1)}\delta(2,1)$ ($A^{(c)}_{(1,1)}$ being the scale factor along X) is very close to the Eötvös ratio;
- δ_z, a small fraction of $\delta(2,1)$, is in principle too small to be estimated but is included in the model to check the absence of anomaly;
- S_{xx} and S_{xz} are components of the matrix [S] which is the symmetric part of [T] − [In];
- Δ'_x (close to Δ_x) and Δ'_z (close to Δ_z) are "effective" components of the off-centring taking into account the sensitivity matrix;
- $\sum_{j=0}^{3} \alpha_j (t-t_0)^j$ is an empirical polynomial term aiming to absorb the effect of the bias and its slow drift (mainly due to thermal effects).

3.2 Results

The final results of the MICROSCOPE mission are based on eighteen sessions for SUEP and nine sessions for SUREF (Touboul et al. 2022b). A few sessions were discarded because of non-linearities at the beginning of the mission (before the control loop's electronics was upgraded) and a few others were discarded because of rare anomalies.

In practice, instrumental defects are parameterised by the $\overrightarrow{b}_1^{(d)}$ and $\overrightarrow{\Delta}$ vectors, as well as the $\left[A^{(d)}\right]$ and $\left[A^{(c)}\right]$ matrices in Eq. (3.3), with only some of their components impacting the projected acceleration (Rodrigues et al. 2022a,b). The estimation of Δ'_x and Δ'_z uses their couplings with the Earth gravity gradient, whose strong spectral line at $2f_{\rm EP}$ allows for a direct determination in science data based on an accurate Earth gravity model.

The final MICROSCOPE's constraint on the validity of the WEP is (Touboul et al. 2022a)

$$\delta(\mathrm{Ti},\mathrm{Pt}) = [-1.5 \pm 2.3\ (\mathrm{stat}) \pm 1.5\ (\mathrm{syst})] \times 10^{-15}, \tag{3.4}$$

where the statistical error is given at 1σ.

The reference instrument provided a null result, $\delta(\mathrm{Pt},\mathrm{Pt}) = [0.0 \pm 1.1\ (\mathrm{stat}) \pm 2.3\ (\mathrm{syst})] \times 10^{-15}$, showing no sign of unaccounted systematic errors in Eq. (3.4). As expected from its higher sensitivity, SUREF's result has a smaller statistical error than SUEP's. On the opposite, it has higher systematic errors (dominated by thermal effects), since they were estimated with less optimal sessions than SUEP's ones (Rodrigues et al. 2022b).

3.3 Beyond the WEP

MICROSCOPE was the first space-based laboratory dedicated to testing the WEP (Bergé 2023). Beside reaching its main goal, the mission also demonstrated technological advances (e.g. 6-degrees-of-freedom drag-free and attitude control) and provided an experience on the limits of the experiment. Furthermore, it allowed for state-of-the-art bounds on ultra-light dark matter and long-range fifth forces (Bergé et al. 2018). Additionally, it was shown that in principle, a MICROSCOPE-like experiment could constrain short fifth force models and screening mechanisms; nevertheless, MICROSCOPE itself was not designed for those experiments and gave only poor constraints (Bergé et al. 2022; Pernot-Borràs et al. 2021).

References

Bergé, J. 2023, Reports on Progress in Physics, 86, 066901

Bergé, J., Brax, P., Métris, G., et al. 2018, Physical Review Letters, 120, 141101

Bergé, J., Pernot-Borràs, M., Uzan, J.-P., et al. 2022, Classical and Quantum Gravity, 39, 204010

Bessel, F. W. 1832, Ann. Phys. Chem. (Poggendorf), 25, 401-17

Braginskii, V. B. & Panov, V. I. 1971, Zh. Eksp. Teor. Fiz., 61, 873-879

Chapman, P. K. & Hanson, A. J. 1970, in Proc. Conf. on Experimental Tests of Gravitation Theories, ed. R. W. Davies, JPL TM, 228

Eötvös, L., Pekár, D., & Fekete, E. 1922, Ann. Phys., 68, 11

Everitt, C. W. F., Damour, T., Nordtvedt, K., & Reinhard, R. 2003, Advances in Space Research, 32, 1297

Ishak, M. 2019, Living Reviews in Relativity, 22

Liorzou, F., Touboul, P., Rodrigues, M., et al. 2022, Classical and Quantum Gravity, 39, 204002

Pernot-Borràs, M., Bergé, J., Brax, P., et al. 2021, Physical Review D, 103, 064070

Rodrigues, M., Touboul, P., Métris, G., et al. 2022a, Classical and Quantum Gravity, 39, 204004

Rodrigues, M., Touboul, P., Métris, G., et al. 2022b, Classical and Quantum Gravity, 39, 204006

Roll, P. G., Krotkov, R., & Dicke, R. 1964, Annals Phys., 26, 442-517

Schlamminger, S., Choi, K.-Y., Wagner, T. A., Gundlach, J. H., & Adelberger, E. G. 2008, Physical Review Letters, 100, 041101

Touboul, P., Métris, G., Rodrigues, M., et al. 2019, Classical and Quantum Gravity, 36, 225006

Touboul, P., Métris, G., Rodrigues, M., et al. 2017, Physical Review Letters, 119, 231101

Touboul, P., Métris, G., Rodrigues, M., et al. 2022a, Physical Review Letters, 129, 121102

Touboul, P., Métris, G., Rodrigues, M., et al. 2022b, Classical and Quantum Gravity, 39, 204009

Touboul, P., Rodrigues, M., Métris, G., et al. 2022c, Classical and Quantum Gravity, 39, 204001

Viswanathan, V., Fienga, A., Minazzoli, O., et al. 2018, MNRAS, 476, 1877-1888

Wagner, T. A., Schlamminger, S., Gundlach, J. H., & Adelberger, E. G. 2012, Classical and Quantum Gravity, 29, 184002

Will, C. M. 2014, Living Reviews in Relativity, 17

Williams, J. G., Turyshev, S. G., & Boggs, D. H. 2012, Classical and Quantum Gravity, 29, 184004